OPEN ACCESS
IOP Publishing
Measurement Science and Technology
Meas. Sci. Technol. **31** (2020) 065013 (10pp)
https://doi.org/10.1088/1361-6501/ab7359

Thermal expansion and compressibility of single-crystal silicon between 285 K and 320 K

Guido Bartl, Clemens Elster, Jörg Martin, René Schödel, Michael Voigt and Alexander Walkov

Physikalisch-Technische Bundesanstalt, Braunschweig and Berlin, Germany

E-mail: guido.bartl@ptb.de

Received 23 October 2019, revised 24 January 2020
Accepted for publication 6 February 2020
Published 3 April 2020

Abstract

The absolute length of a single-crystal silicon gauge block was measured by interferometry in the temperature range between 285 K and 320 K and at different air pressures from atmospheric conditions down to 10^{-5} hPa. From the obtained dataset, the coefficient of thermal expansion (CTE) was determined as well as the compressibility—or the bulk modulus—of single-crystal silicon in consideration of a systematic correction of the refractometer used. As the choice of the underlying model for the evaluation is not unambiguous, a Bayesian model averaging approach was applied to take into account possible model errors in the uncertainty evaluation. The result of the CTE is not only in agreement with the recommended reference data of CODATA, but provides a standard uncertainty of less than 1×10^{-9} K^{-1}, which is less than half the uncertainty stated so far in the relevant temperature range.

Keywords: single-crystal silicon, thermal expansion, compressibility, bulk modulus, interferometry, length measurement

(Some figures may appear in colour only in the online journal)

Supplementary material for this article is available online

1. Introduction

Justified by the need for a reference material for thermal expansion measurements of high precision (e.g. [1, 2] and others), there have been a variety of thermal expansion measurements on silicon over a wide temperature range in the past. Due to its diamond-like crystallographic structure, single-crystal silicon provides isotropy with regard to thermal expansion. Moreover, the industry-driven availability of high-purity material makes silicon an ideal candidate—in contrast to technical-application specimens as described in [3]. Also the recent revision of the '*Mise en pratique* for the definition of the metre in the SI'[4] refers to the lattice spacing of silicon as a basis for secondary methods of realising the metre on the nanometre scale. In this context, knowledge of the CTE can be used in the secondary realisation of the length as described in the updated *Mise en pratique*. Overview reports on thermophysical properties, e.g. [5], usually refer to [6], which presents a compilation of several measurement results from different laboratories covering the temperature range from 90 K up to 850 K and has acted as a reference source of thermal expansion data of silicon ever since its publication[1]. Some of the involved data were taken from [8–10], and a later extension of the temperature range up to 1300 K [11] was taken into account afterwards [12]. In the scope of a programme to establish a thermal expansion standard, part of the upper temperature range above 600 K has been reinvestigated after experimental refinements [13]. The results of thermal expansion measurements between 7 K and 293 K have been presented in [14] in comparison with data from the National

[1] Standard reference data recommended by CODATA [7].

Metrology Institute of Japan (NMIJ) and the Jet Propulsion Laboratory (JPL) [15], indicating a systematic deviation from the CODATA reference data. Data of the highest precision in quite a limited temperature range close to 20 °C have been reported earlier in [16], accompanied by the determination of the material's compressibility. In contrast to the dilatometric measurements from other works, the results in [14, 16] are derived from absolute length measurements. The work is followed up by the present study of thermal expansion extending the temperature range to 320 K with a reduced measurement uncertainty. Moreover, the simultaneous determination of the compressibility of silicon resolves the discrepancy of the previous results stated in [16] and match with data from the literature [17] (referring to [18, 19]).

The results in this work originate from measurements carried out on a single-crystal silicon sample, the dimensions of which are 197 mm × 35 mm × 9 mm (see figure 1). The original high-purity crystal ingot—called #41969/05—was grown by Wacker Siltronic GmbH, Germany, using the float-zone technique in an argon atmosphere without any doping [20]. The gauge block sample was cut from the dislocation-free '0-zone' region along the ⟨100⟩ direction between the axial crystal positions at 75 cm and 103 cm (see figure 2 in [20]). The two small end faces with a 35 mm × 9 mm cross section were lapped to achieve optical quality and parallel orientation perpendicular to the long axis. The sample used in [16] was cut from the same crystal ingot out of the same '0-zone' region and axial position and has the same dimensions.

The measurement data were analysed using a novel technique recently presented in [21]. Being a quantity that is computed via a derivative, the coefficient of thermal expansion turns out to be quite sensitive to the concrete model that is chosen to fit the thermal expansion measurements. In [21], a new approach, based on Bayesian model averaging, was therefore proposed that allows various models to be treated and compared in one framework. By taking model errors into account, a more coherent inference can be conducted. Furthermore, via the computation of model probabilities, a more direct comparison can be performed.

2. Experimental setup

The details of the Twyman-Green-type imaging interferometer used (figure 2) have already been described comprehensively in [22]. For the length measurements, the light of three stabilised lasers (wavelengths: 532 nm, 633 nm and 780 nm) is successively fed into the interferometer beam path. The gauge-block-shaped sample as well as the refractometer cell, which is used for the interferometric in-situ determination of the air refractive index [23–25], are placed on the sample platform (similar to [16]). The mirror behind the refractometer cell reflects the transmitted light towards the camera so that the cell is passed twice. The full field of view is imaged onto the camera, by which a sequence of ten interferograms is recorded, enabling the averaged five-frame phase-shifting approach [22, 26] applied for the evaluation of the interference phase. In the focus of the exit collimator, an aperture stop

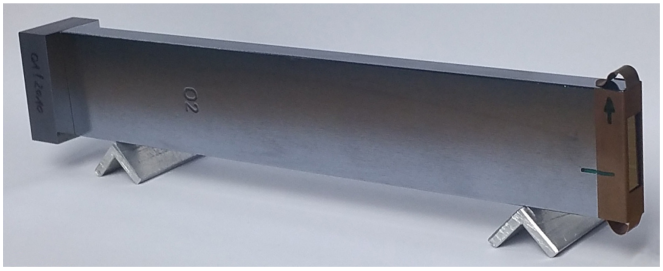

Figure 1. Close-up view of the silicon sample. The dimensions of the gauge-block-shaped body are 197 mm × 35 mm × 9 mm. At the back end face, the optically flat silicon reference plate is attached by wringing. At the front end face, a metal frame is softly clamped onto the gauge block to mask edge damage and to facilitate the edge detection within the interference pattern recorded by the camera.

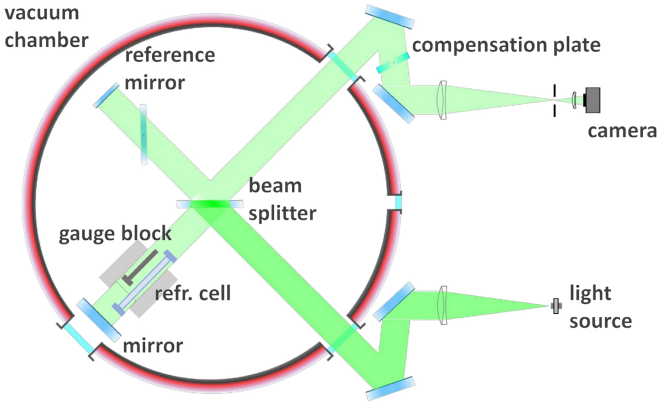

Figure 2. Sketch of the interferometer.

blocks parasitic reflections from surfaces in the beam path (e.g. chamber windows) leaving the interferometer. A wedged glass plate in the exit beam path compensates for wavelength-dependent images shifts so that the beam locations are almost identical for all three wavelengths applied in the measurements [27].

In order to achieve constant thermal conditions, the interferometer is set up in a pressure-tight/vacuum chamber enveloped by a tubing system with water from a thermostat flowing through it. To monitor the temperature of the sample, three thermocouple sensors [28] are attached to its surface at different locations. The reference junction of each sensor couple is fixed to a copper block, the absolute temperature of which is measured by a Pt-25 resistance thermometer calibrated at the fixed points of water and gallium according to the ITS-90[2] [29]. This operating principle requires the thermocouple sensors to only measure small temperature differences, i.e. a few tens of millikelvins at maximum. Six additional thermocouple sensors are positioned around the sample and the refractometer cell to keep track of the temperature homogeneity of the surrounding gas medium when the chamber is not evacuated. The pressure of the gas, i.e. air, is measured by traceably calibrated sensors of the *MENSOR CPT6100* or *CERAVAC CTR 91* (1 Torr) type, depending on the actual pressure ranges. The air is kept dry by means of a cooling trap

[2] International Temperature Scale of 1990.

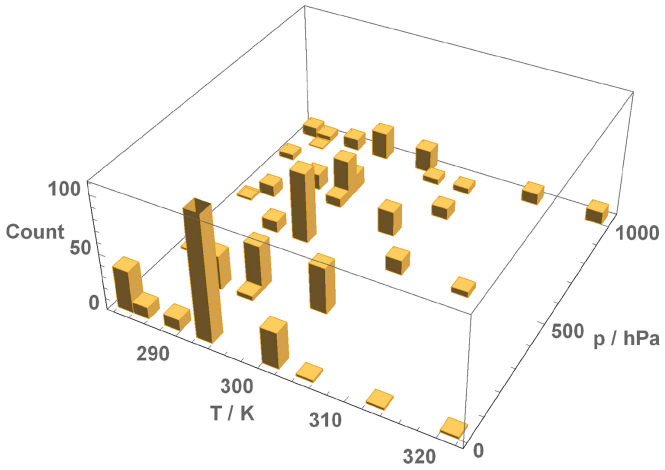

Figure 3. Number of measurements distributed within the parameter intervals of temperature and pressure. The clipped maximum around T=293.15 K and $p<10^{-1}$ hPa amounts to approximately 500 measurements.

consisting of a tube which is dipped into a Dewar vessel filled with liquid nitrogen. The vacuum state, i.e. less than 10^{-4} hPa, is monitored by a sensor of the type *IONIVAC IE 20*.

3. Measurement strategy

The investigation of the thermal expansion and the compressibility based on absolute length measurements can be realised by a convenient temporal sequence of temperature and pressure steps. A specific order is not necessary. Therefore, the parameter space of temperature T and pressure p has been sampled adequately within the intervals of 285 K < T < 320 K and 10^{-5} hPa < p < 1030 hPa, respectively. The histogram in figure 3 shows the corresponding distribution of measurements which have arisen from experimental circumstances or practical constraints. For instance, keeping the chamber at temperatures above 300 K for something more than a day leads to condensation liquid appearing on the inner side of the windows of the chamber. Therefore, the measurement point density is kept smaller in this temperature region. The data acquisition took place over a period of approximately three months. After each change of the temperature or the pressure, a waiting period of at least half a day was necessary to achieve thermal equilibrium again. Length measurements were only carried out when the temperature drift was close to zero. Near room temperature, i.e. 20 °C, also the measured temperature differences between the different sensor locations were negligibly small. Away from this reference temperature, however, spatial temperature differences of up to 10 mK may occur, which have to be taken into account in the temperature evaluation and the corresponding uncertainty analysis.

4. Data evaluation

The principle of the interferogram analysis, i.e. the evaluation chain from the camera images to the resulting length values, has been described in detail in [22]. A typical interferogram is shown in figure 4. The interference phase is calculated

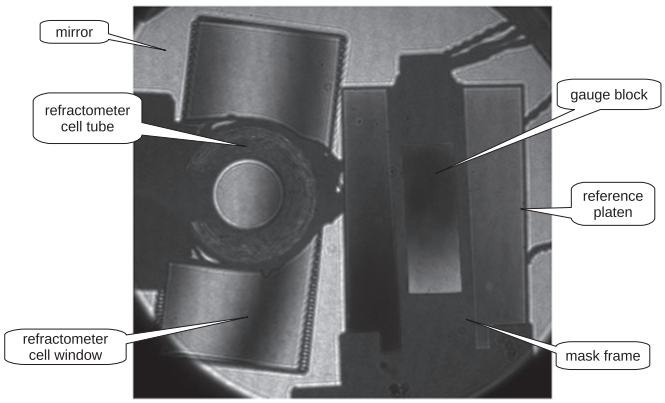

Figure 4. A typical interferogram captured by the camera. The structure on the right-hand side is the gauge block with its reference plate. The refractometer cell is located on the left.

from a sequence of phase-shifted interferograms so that the phase difference ϕ between regions of interest on the sample's front surface in relation to the attached reference plate can be determined. For each wavelength of the light used, the length of the sample is then calculated by

$$L = \frac{\lambda}{2n} \cdot \left(N + \frac{\phi}{2\pi} \right) \tag{1}$$

in terms of the measured integral and fractional orders of interference N and $\phi/2\pi$, respectively, the vacuum wavelength λ and the refractive index n of the surrounding (gas) medium. An estimate for the value of N is obtained from a separate mechanical measurement with an uncertainty in the order of 1 µm in combination with an extrapolation to the actual temperature and pressure conditions during the measurement. The method of exact fractions is then applied to the measurement results from the different laser wavelengths to find the correct order of interference N [23].

If the pressure is below 1 hPa, the refractive index n is evaluated by the modified Edlén formula [30] involving the measured gas parameters, which yields sufficient accuracy in this pressure range [31]. At higher pressures, the phase difference between regions of interest corresponding to the beam path through the evacuated refractometer cell and the path along the cell is determined analogously to the described length evaluation. This is done in order to measure the actual refractive index *in situ*. In this case, the result from Edlén's formula is only considered as the required prior knowledge. As the windows of the refractometer cell implicate non-uniform geometric conditions depending on the location in the field of view, a correction of the accompanying optical path length difference has to be applied. This is realised by determining the optical path length difference with the evacuated refractometer cell being in the evacuated vacuum chamber. The resulting value is considered as a corrective offset for the measurements in air. As these vacuum measurements were carried out repeatedly during the entire measurement period, the correction is monitored continuously and no systematic dependence on the actual temperature is found. Moreover, measurements at pressures above 50 hPa require an additional

Table 1. Example uncertainty budget of the contributing quantities' standard uncertainties at 20 °C and 10^{-4} hPa. Further contributions smaller than 0.001 nm are omitted for clarity.

Quantity	Standard uncertainty	Sensitivity coefficient	Contribution to the length uncertainty
Sample phase fraction	0.000 63 rad	4.24×10^{-08} m rad^{-1}	0.027 nm
Sample ROI position	0.1 pixel	1.80×10^{-10} m pixel^{-1}	0.018 nm
Reference plate deformation	0.012 27 rad	4.24×10^{-08} m rad^{-1}	0.520 nm
Gas pressure	2.19E-05 hPa	-5.33×10^{-08} m hPa^{-1}	0.001 nm
Gas dew point	7.9 K	7.16×10^{-12} m K^{-1}	0.057 nm
Laser wavelength	1×10^{-17} m	370896.8 m m^{-1}	0.004 nm
Autocollimation	4×10^{-11} m	1 m m^{-1}	0.040 nm
Temperature-induced optics deformation	1×10^{-10} m	1 m m^{-1}	0.100 nm
Sample temperature (incl. calibration of Pt25 and thermocouples)	0.000 68 K	5.04×10^{-07} m K^{-1}	0.342 nm
Sample temperature inhomogeneity	0.000 20 K	5.04×10^{-07} m K^{-1}	0.100 nm
Combined standard uncertainty			0.7 nm

correction due to stress-induced optical path length changes in the windows of the refractometer cell [24, 25, 32]. This is because the optical paths through and along the glass tube are affected differently. Since—unlike the pressure-induced stress—temperature-dependent changes of the refractive index of the cell windows are sufficiently homogeneous across the windows, there is no need for a temperature-dependent correction.

At this point, the subsequent processing of the collected length data at different temperatures and pressures combined with a coherent evaluation of the corresponding measurement uncertainty is in the foreground. The approach used in the following sections is founded on the absolute length values and their individual uncertainty budgets, the latter of which are important due to significant pairwise correlations. Two example uncertainty budgets representing different experimental conditions are listed in tables 1 and 2. These examples represent the ideal case of 20 °C and vacuum, which provide very stable experimental conditions, and a worse case at elevated temperature and atmospheric pressure causing larger temperature gradients. Some of the involved uncertainty contributions are negligibly small (e.g. the CO_2 content of the air) and, therefore, omitted for clarity, here. Other quantities contribute significant correlations to the evaluation of the CTE and the compressibility. These correlations of different length measurements are, for instance, due to the common calibration of the temperature sensors or commonly applied corrections. It is to be noted that the uncertainty contributions of the corrections considering the influence of surface roughness, optical phase shift and wringing contact are intentionally set to zero. Even though, in fact, they contribute a dominating portion (i.e. several nanometres) to the total uncertainty of each individual absolute length value, the uncertainty variation within the parameter space of temperature and pressure become clearer without them. Zeroing these contributions is justified, because the uncertainty of the results of the thermal expansion and the compressibility are not affected. The reason is, that both quantities are differentially deduced from the length data, which are correlated with regard to the mentioned corrections.

4.1. Model equation for L(T, p)

In order to consider the two-dimensional parameter space of the length data $L(T, p)$, an appropriate model function has to be applied in the evaluation via a least squares regression. Therefore, we start with the total differential of $L(T, p)$ which is given by

$$\mathrm{d}L = \frac{\partial L}{\partial T}\,\mathrm{d}T + \frac{\partial L}{\partial p}\,\mathrm{d}p. \tag{2}$$

Considering a homogeneous material like pure single-crystal silicon, the coefficient of linear thermal expansion at constant pressure p is

$$\alpha_l = \frac{1}{L}\,\frac{\partial L}{\partial T}, \tag{3}$$

and the isothermal compressibility κ as the reciprocal of the isothermal bulk modulus K is defined as

$$\kappa = \frac{1}{K} = -\frac{1}{V}\frac{\partial V}{\partial p} = -\frac{3}{L}\,\frac{\partial L}{\partial p}. \tag{4}$$

With these relations, equation (2) can be rearranged as

$$\frac{1}{L}\,\mathrm{d}L = \alpha_l\,\mathrm{d}T - \frac{\kappa}{3}\,\mathrm{d}p. \tag{5}$$

While α_l is assumed to change little with pressure[3], the temperature influence on κ is expected to be negligible in the covered temperature interval. Hence, a linear dependence of α_l on the pressure is considered by

$$\alpha_l(T,p) = \alpha(T) + \tilde{\alpha}\cdot p, \tag{6}$$

where $\alpha(T)$ is the coefficient of linear thermal expansion at $p = 0$ and $\tilde{\alpha}$ is a constant parameter. Actually, considering the temperature dependence of the compressibility [34], the same approach could also be applied to κ, but the principle of

[3] In analogy to Murnaghan's ansatz for the pressure dependency of the bulk modulus in the derivation of *Murnaghan's equation of state* [33].

Table 2. Example uncertainty budget of the contributing quantities' standard uncertainties at 48 °C and 1007 hPa. Although contributing little to the total uncertainty, the entries 'gas pressure' and 'refractometer compressibility' are listed due to their key role in the evaluation. Further contributions smaller than 0.001 nm are omitted for clarity.

Quantity	Standard uncertainty	Sensitivity coefficient	Contribution to the length uncertainty
Sample phase fraction	0.000 63 rad	4.23×10^{-08} m rad^{-1}	0.027 nm
Sample ROI position	0.1 pixel	2.01×10^{-10} m pixel^{-1}	0.020 nm
Reference plate deformation	0.016 58 rad	4.23×10^{-08} m rad^{-1}	0.702 nm
Refractometer tube length	5×10^{-07} m	0.00012 m m^{-1}	0.058 nm
Refractometer thermal expansion	3.12×10^{-07} K^{-1}	0.001 38 m K	0.431 nm
Refractometer compressibility	1.60×10^{-11} Pa^{-1}	−0.00010 m Pa	0.000 nm
Gas temperature (incl. calibration of Pt25 and thermocouples)	0.0260 K	2.64×10^{-11} m K^{-1}	0.001 nm
Gas pressure (incl. sensor calibration)	0.06 hPa	4.51×10^{-16} m hPa^{-1}	0.000 nm
Refractometer phase fraction	0.000 63 rad	-1.99×10^{-08} m rad^{-1}	0.013 nm
Refractometer ROI position	0.1 pixel	-4.25×10^{-11} m pixel^{-1}	0.004 nm
Refractometer zero correction	5×10^{-10} m	0.47 m m^{-1}	0.235 nm
Refractometer window compression	4×10^{-10} m	−0.47 m m^{-1}	0.190 nm
Laser wavelength	1×10^{-17} m	370924.8 m m^{-1}	0.004 nm
Autocollimation	4×10^{-11} m	1 m m^{-1}	0.040 nm
Temperature-induced optics deformation	1×10^{-10} m	1 m m^{-1}	0.100 nm
Sample temperature (incl. calibration of Pt25 and thermocouples)	0.002 59 K	5.05×10^{-08} m K^{-1}	1.306 nm
Sample temperature inhomogeneity	0.001 54 K	5.05×10^{-07} m K^{-1}	0.777 nm
Combined standard uncertainty			1.8 nm

the resulting model equation of $L(T,p)$ would not be affected apart from a substitution of the corresponding parameter names. Proceeding with the integration of equation (5) and introducing the reference length and temperature, L_{ref} and T_{ref}, respectively, lead to

$$\int_{L_{\mathrm{ref}}}^{L} \frac{1}{L'}\,\mathrm{d}L' = \int_{T_{\mathrm{ref}}}^{T} \alpha_l(T',p)\,\mathrm{d}T' - \int_0^p \frac{\kappa}{3}\,\mathrm{d}p' \qquad (7)$$

$$\Leftrightarrow L = L_{\mathrm{ref}} \cdot \exp\left(\int_{T_{\mathrm{ref}}}^{T} \alpha(T')\,\mathrm{d}T' + \tilde{\alpha}\,p\,(T-T_{\mathrm{ref}}) - \frac{\kappa}{3}\,p,\right) \qquad (8)$$

which can be approximated by a Taylor expansion of the exponential function:

$$L = L_{\mathrm{ref}} \cdot \left(1 + \int_{T_{\mathrm{ref}}}^{T} \alpha(T')\,\mathrm{d}T' + \tilde{\alpha}\,p\,(T-T_{\mathrm{ref}}) - \frac{\kappa}{3}\,p\right). \qquad (9)$$

Finally, there remains the choice of a suitable expression for $\alpha(T)$.

4.2. Model equation for $\alpha(T)$

As for the selection of an appropriate model for the CTE $\alpha(T)$, there are two approaches which are considered in the following. In [14], the evaluation of the CTE of single-crystal silicon covering a temperature range from 7 K to 293 K has been reported. Because of the nonlinear behaviour of the CTE of single-crystal silicon in the respective large temperature interval (particularly at cryogenic temperatures), a simple polynomial fitting was not adequate. Alternatively, a piecewise evaluation of smaller temperature intervals by polynomials as used in [22] was at the very least not so pleasant due to the incoherent treatment of the data. Moreover, the required polynomial degrees may vary and an extrapolation beyond the limits of the temperature range covered by the actual measurements is only reasonable based on a physically motivated model. Therefore, the appropriate approach from [35]—already introduced in [36]—was applied, in which the CTE is modelled by an empirical nonlinear function based on so-called Einstein terms.

However, in the current case of a limited temperature range between 285 K and 320 K, both model approaches appear to be applicable, which raises the question of how the uncertainty is affected by the decision for or against one particular model. Therefore, the method of Bayesian model averaging has been adapted and applied to the evaluation of the CTE and its uncertainty based on measured absolute length data [21]. This approach (in contrast to [14] or [37]) does not require a commitment to a specific model but allows several competing models to be incorporated and compared in one framework. Starting from *a priori* probabilities for each considered model, which can for instance all be chosen equally, these probabilities are updated in the light of the data using Bayes' theorem. As an outcome, one obtains *a posteriori* probabilities for each model, which allow a direct comparison. Moreover, deduced estimates and uncertainties in Bayesian model averaging avoid inconsistencies between models and take model errors into account. This is of particular importance in the context of CTE determination as the quantity of interest is often obtained via the derivation of fitted curves—a badly behaved operation that might lead to distinct discrepancies between two models yielding practically indistinguishable fits on the measurement data.

Accordingly, $\alpha(T)$ is represented by the polynomial expression

$$\alpha_{\mathrm{P}}(T) = \zeta_1 + \zeta_2 \cdot (T - T_{\mathrm{ref}}) + \zeta_3 \cdot (T - T_{\mathrm{ref}})^2 \qquad (10)$$

with the parameters ζ_1, ζ_2 and ζ_3 as well as by the nonlinear Einstein-term expression

$$\alpha_{\mathrm{E}}(T) = \xi \cdot \left(\frac{\theta}{T}\right)^2 \cdot \frac{e^{\theta/T}}{\left(e^{\theta/T} - 1\right)^2} \qquad (11)$$

with the parameters ξ and θ in the evaluation of the results in the following sections. Here, the explicit proportionality of α and κ (cf. [36]) is omitted for simplicity and implicitly considered by the parameter ξ. The respective number of polynomial degrees and Einstein terms is chosen so that the model functions can sufficiently represent the experimental data without over- or underfitting them.

5. Results and uncertainty

With the two selected variants of $\alpha(T)$, the model prototype $L(T,p)$ from equation (9) finally becomes

$$\begin{aligned} L_{\mathrm{P}}(T,p) = {} & L_{20} + \zeta_1' \cdot (T - T_{\mathrm{ref}}) + \zeta_2' \cdot (T - T_{\mathrm{ref}})^2 \\ & + \zeta_3' \cdot (T - T_{\mathrm{ref}})^3 + \tilde{\alpha}_{\mathrm{P}}' \cdot p \cdot (T - T_{\mathrm{ref}}) \\ & - \frac{\kappa_{\mathrm{P}}'}{3} \cdot p \end{aligned} \qquad (12)$$

and

$$\begin{aligned} L_{\mathrm{E}}(T,p) = {} & L_0 + \xi' \cdot \frac{\theta}{e^{\theta/T} - 1} \\ & + \tilde{\alpha}_{\mathrm{E}}' \cdot p \cdot (T - T_{\mathrm{ref}}) - \frac{\kappa_{\mathrm{E}}'}{3} \cdot p, \end{aligned} \qquad (13)$$

respectively. The reference temperature is set to $T_{\mathrm{ref}} = 293.15$ K and the quantities $L_{20} \equiv L(T_{\mathrm{ref}}, 0\ \mathrm{hPa})$ and $L_0 \equiv L(0\ \mathrm{K}, 0\ \mathrm{hPa})$ as well as $\tilde{\alpha}_{\mathrm{P}}' = L_{20} \cdot \tilde{\alpha}$, $\tilde{\alpha}_{\mathrm{E}}' = L_0 \cdot \tilde{\alpha}$, $\kappa_{\mathrm{P}}' = L_{20} \cdot \kappa$, $\kappa_{\mathrm{E}}' = L_0 \cdot \kappa$, $\xi' = L_0 \cdot \xi$, θ, $\zeta_1' = L_{20} \cdot \zeta_1$, $\zeta_2' = L_{20} \cdot \frac{\zeta_2}{2}$ and $\zeta_3' = L_{20} \cdot \frac{\zeta_3}{3}$ are treated as fit parameters. The parameters of both models, (12) and (13), are estimated via a weighted least squares regression of the measured data to derive the thermal expansion and the compressibility in a second step. The resulting fit parameters are

$$\begin{aligned} L_{20} &= 197.4246884 \times 10^{-3}\,\mathrm{m} \\ \zeta_1' &= 504.5518 \times 10^{-9}\,\mathrm{m\ K^{-1}} \\ \zeta_2' &= 886.6378 \times 10^{-12}\,\mathrm{m\ K^{-2}} \\ \zeta_3' &= -1.6983 \times 10^{-12}\,\mathrm{m\ K^{-3}} \\ \kappa_{\mathrm{P}}' &= 200.8658 \times 10^{-12}\,\mathrm{m\ hPa^{-1}} \\ \tilde{\alpha}_{\mathrm{P}}' &= 11.2988 \times 10^{-15}\,\mathrm{m\ K^{-1} hPa^{-1}} \end{aligned}$$

with the corresponding covariance matrix

$$\mathbf{C}_{\mathrm{P}} = \begin{pmatrix} 6.5568 \times 10^{-20} & -1.2090 \times 10^{-22} & -3.0753 \times 10^{-23} & 1.0780 \times 10^{-24} & 1.3675 \times 10^{-23} & 9.6366 \times 10^{-26} \\ -1.2090 \times 10^{-22} & 1.2399 \times 10^{-21} & -2.6937 \times 10^{-24} & -3.5859 \times 10^{-25} & -9.7732 \times 10^{-25} & -3.7448 \times 10^{-25} \\ -3.0753 \times 10^{-23} & -2.6937 \times 10^{-24} & 4.3391 \times 10^{-24} & -1.5841 \times 10^{-25} & 3.6623 \times 10^{-25} & 5.8101 \times 10^{-27} \\ 1.0780 \times 10^{-24} & -3.5859 \times 10^{-25} & -1.5841 \times 10^{-25} & 7.7690 \times 10^{-27} & -1.1194 \times 10^{-26} & -5.9500 \times 10^{-28} \\ 1.3675 \times 10^{-23} & -9.7732 \times 10^{-25} & 3.6623 \times 10^{-25} & -1.1194 \times 10^{-26} & 6.6939 \times 10^{-25} & 1.6126 \times 10^{-27} \\ 9.6366 \times 10^{-26} & -3.7448 \times 10^{-25} & 5.8101 \times 10^{-27} & -5.9500 \times 10^{-28} & 1.6126 \times 10^{-27} & 1.2110 \times 10^{-27} \end{pmatrix}$$

as well as

$$\begin{aligned} L_0 &= 197.3723301 \times 10^{-3}\,\mathrm{m} \\ \kappa_{\mathrm{E}}' &= 200.9035 \times 10^{-12}\,\mathrm{m\ hPa^{-1}} \\ \tilde{\alpha}_{\mathrm{E}}' &= 12.5056 \times 10^{-15}\,\mathrm{m\ K^{-1} hPa^{-1}} \\ \xi' &= 867.6807 \times 10^{-9}\,\mathrm{m\ K^{-1}} \\ \theta &= 767.8031\ \mathrm{K} \end{aligned}$$

with the covariance matrix

$$\mathbf{C}_{\mathrm{E}} = \begin{pmatrix} 8.7040 \times 10^{-16} & 3.8960 \times 10^{-21} & -1.0459 \times 10^{-22} & 1.6974 \times 10^{-17} & 1.5225 \times 10^{-8} \\ 3.8960 \times 10^{-21} & 6.5357 \times 10^{-25} & 7.5529 \times 10^{-28} & 7.7558 \times 10^{-23} & 6.8789 \times 10^{-14} \\ -1.0459 \times 10^{-22} & 7.5529 \times 10^{-28} & 1.1645 \times 10^{-27} & -3.8447 \times 10^{-24} & -2.7061 \times 10^{-15} \\ 1.6974 \times 10^{-17} & 7.7558 \times 10^{-23} & -3.8447 \times 10^{-24} & 3.4663 \times 10^{-19} & 3.0450 \times 10^{-10} \\ 1.5225 \times 10^{-8} & 6.8789 \times 10^{-14} & -2.7061 \times 10^{-15} & 3.0450 \times 10^{-10} & 0.2700 \end{pmatrix}.$$

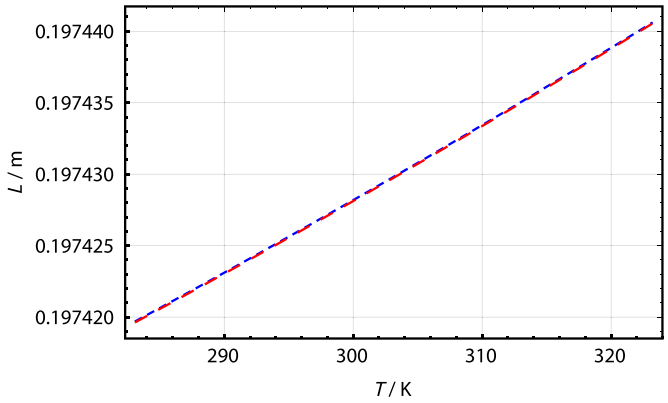

Figure 5. The dashed blue and red lines show the fitted curve $L(T)$ according to equation (13) at 0 Pa and 1000 hPa, respectively.

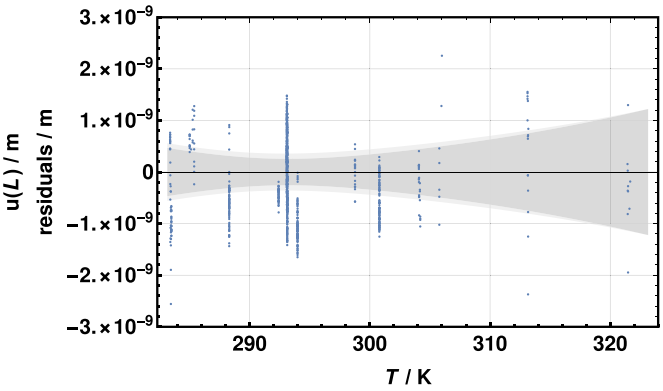

Figure 6. The dark and light grey areas show the standard uncertainty $u(L)$ of the fitted curve $L(T)$ according to equation (13) at 0 Pa and 1000 hPa, respectively. The blue dots represent the residuals of each measured value considered in the weighted least squares regression. Please note that, although plotted versus temperature only, the data points represent the entire pressure range from vacuum to atmospheric pressure.

Please note that the physical units in the entries of the covariance matrices are omitted for simplicity only. Moreover, the order of the entries is in accordance with the order of the listed results of the fit parameters. It must be emphasised that weighting of the optimisation is done based on the full covariance matrix of the entire dataset—in contrast to simply using the reciprocal squared standard uncertainties as can be found in most applications. Doing so coherently takes into account the significant mutual correlation between the data points and yields the correct output uncertainties of the fit parameters of both models.

As an example, the result of the Einstein-term model is shown in figure 5 for the two cases of vacuum and atmospheric pressure. Since the pressure dependence of the length is significantly smaller compared to the effect of temperature changes on the chosen scale, the two plotted lines are hard to distinguish. The corresponding standard uncertainty is shown in figure 6 together with the related residuals. The present results have been evaluated based on the measured temperatures according to the ITS-90. A correction with regard to thermodynamic temperatures [38] has not been applied.

5.1. Thermal expansion

The expression for the thermal expansion can be derived following equation (3) from both the above-mentioned fits. As outlined in section 4.2, the method of Bayesian model averaging, which has been described in [21], is applied in this evaluation to take into account competing model variants. Therefore, the two selected models are averaged considering the corresponding *a posteriori* model probabilities:

$$\hat{\alpha}(T,p) = P_{\mathrm{P}} \cdot \frac{1}{L_{\mathrm{P}}(T,p)} \frac{\partial L_{\mathrm{P}}(T,p)}{\partial T} + P_{\mathrm{E}} \cdot \frac{1}{L_{\mathrm{E}}(T,p)} \frac{\partial L_{\mathrm{E}}(T,p)}{\partial T}, \tag{14}$$

where L_{P} and L_{E} are evaluated with the parameters specified in the previous section. For the computation of posterior probabilities, we followed the same strategy as in [21]. Using data from [16] as prior knowledge for scaling, we found posterior model probabilities $P_{\mathrm{E}} = 65.9$ % and $P_{\mathrm{P}} = 34.1$ % for the data presented in this work. These are close to the values found in [21]. The resulting course of the thermal expansion depending on the temperature based on the averaged model is shown in figure 7 and the difference of the models $\alpha_{\mathrm{P}}(T,p)$ and $\alpha_{\mathrm{E}}(T,p)$ is negligibly small compared to the corresponding uncertainties. These standard uncertainties of $\alpha_{\mathrm{P}}(T,p)$, $\alpha_{\mathrm{E}}(T,p)$ and $\hat{\alpha}(T,p)$ are plotted in figure 8. While in the middle section of the temperature interval, the uncertainties of $\alpha_{\mathrm{P}}(T,p)$ and $\alpha_{\mathrm{E}}(T,p)$ are almost equal, they differ clearly at the interval edges. This is taken into account by the Bayesian model averaging in the resulting uncertainty of $\hat{\alpha}(T)$. For convenience, some values are listed in table 3.

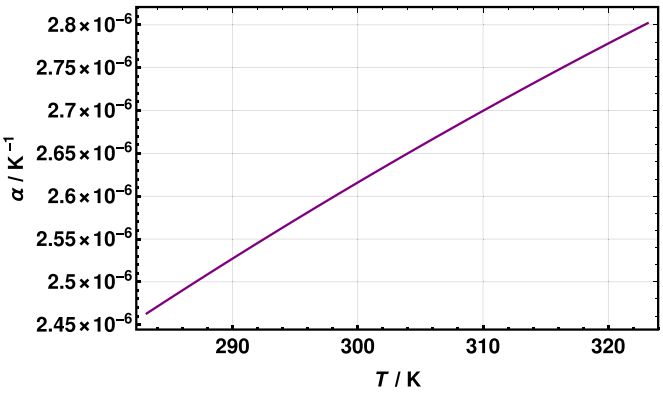

Figure 7. The purple line shows the course of $\hat{\alpha}(T,p)$ according to equation (14) at 0 Pa.

In [6, 7], the compilation of several sources has been prepared which—to our knowledge—presents the lowest uncertainties (in our relevant temperature range mainly based on the data from [9]). Taking this as a reference for the results from the current work enables a comparison which is plotted in figure 9. All data agree well within their corresponding uncertainties over the whole temperature interval, while the current data provide a standard uncertainty, which is smaller by a factor of at least about five compared to the reference data.

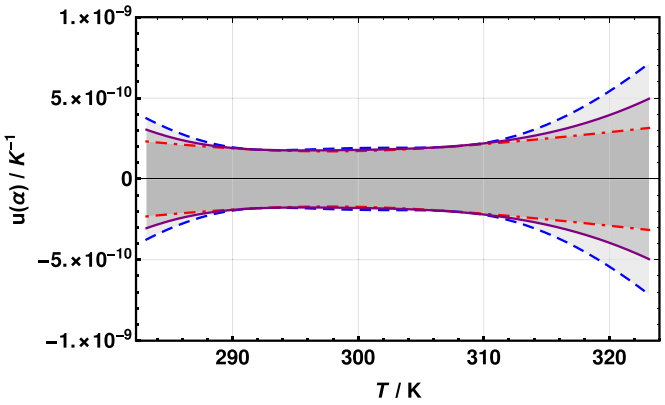

Figure 8. The areas contoured by the dashed blue, dot-dashed red and solid purple lines show the standard uncertainties $u(\alpha_P)$, $u(\alpha_E)$ and $u(\hat{\alpha})$ at 0 Pa, respectively.

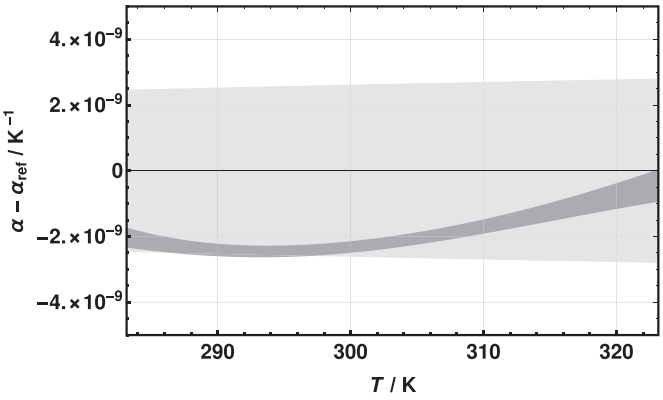

Figure 9. The light grey area shows the standard uncertainty of the currently most precisely known reference data of the coefficient of thermal expansion of silicon in the given temperature range according to [6]. The dark grey area represents the difference of the results from the present work according to equation (14) with regard to these reference data including the corresponding standard uncertainty.

Table 3. Tabulated values of the coefficient of thermal expansion of silicon according to equation (14) at 0 Pa and the corresponding standard uncertainties.

T_{90} / K	t_{90} / °C	α / 10^{-6} K^{-1}	$u(\alpha)$ / 10^{-6} K^{-1}
283.15	10.0	2.4631	0.0003
285.15	12.0	2.4821	0.0003
287.15	14.0	2.5008	0.0002
289.15	16.0	2.5193	0.0002
291.15	18.0	2.5376	0.0002
293.15	20.0	2.5557	0.0002
295.15	22.0	2.5736	0.0002
297.15	24.0	2.5912	0.0002
299.15	26.0	2.6086	0.0002
301.15	28.0	2.6259	0.0002
303.15	30.0	2.6429	0.0002
305.15	32.0	2.6597	0.0002
307.15	34.0	2.6763	0.0002
309.15	36.0	2.6927	0.0002
311.15	38.0	2.7089	0.0002
313.15	40.0	2.7249	0.0003
315.15	42.0	2.7407	0.0003
317.15	44.0	2.7564	0.0003
319.15	46.0	2.7718	0.0004
321.15	48.0	2.7870	0.0004
323.15	50.0	2.8020	0.0005

It must be noted that the current result is related to the current temperature scale, ITS-90, while the reference data refer to the former IPTS-68[4]. A correction would imply a shift by less than 10 mK without a significant effect on the evaluated CTE in the given temperature interval.

The possible pressure dependence of the thermal expansion $\hat{\alpha}$ is taken into consideration in the model. The comparison of the resulting values—for instance at $T = 293.15$ K where the uncertainty is smallest—yields $\hat{\alpha}(293.15\ \text{K}, 0\ \text{hPa}) = 2.55569(18) \times 10^{-6}\ \text{K}^{-1}$ and $\hat{\alpha}(293.15\ \text{K}, 1000\ \text{hPa}) = 2.55567(21) \times 10^{-6}\ \text{K}^{-1}$. Hence, in the limited intervals of temperature and pressure covered in this work, this example does not reveal a significant pressure dependence with regard to the relevant measurement uncertainty. As a consequence, in the application of interferometry on gauge blocks, it is also permissible to apply the coefficient of thermal expansion determined in vacuum for measurements in atmospheric conditions without any further correction.

[4] International Practical Temperature Scale of 1968.

5.2. Compressibility

In [16], the compressibility κ was derived from measured length data at different pressures between vacuum and atmospheric pressure while keeping the temperature very close to 20 °C. In the present case, the length measurements are distributed widely in the parameter space of temperature and pressure, and the model equations (12) or (13) take both parameters inherently into account. Proceeding analogously to section 5.1 one gets the model average $\hat{\kappa}$ of the compressibility of single-crystal silicon. The numerical result at 20 °C and atmospheric pressure is

$$\hat{\kappa} = 1.018(5) \times 10^{-11}\ \text{Pa}^{-1} \tag{15}$$

or, consequently, noted as the bulk modulus

$$K = \frac{1}{\hat{\kappa}} = 98.3(5) \times 10^{9}\ \text{Pa}. \tag{16}$$

Obviously this value of κ markedly differs from the previous result published in [16] and, moreover, is in close agreement with earlier low-uncertainty results from the literature quoted there [18, 19]. The suspected explanation that material differences cause the deviation may not be the real reason. Instead, from today's point of view, there might be another main cause. In the evaluation in [16], the required correction of stress-induced optical path length changes in the refractometer windows [24, 25] was unknown and could therefore not be taken into account. This interpretation is supported by the fact that the result of this work would also be close to the old (wrong)

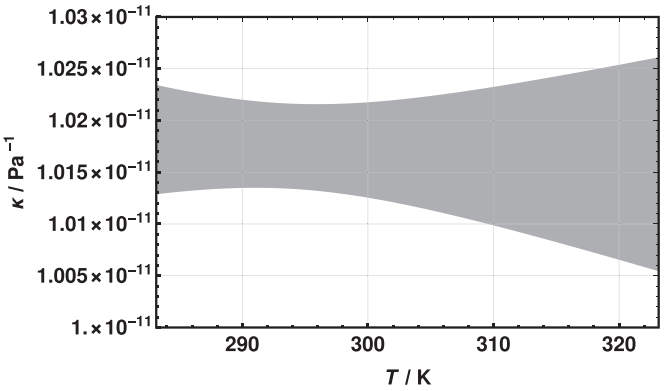

Figure 10. The dark grey area represents the result of $\hat{\kappa}$ at atmospheric pressure including the corresponding standard uncertainty.

value, if the correction of the window stress were omitted. A temperature-dependent change of the bulk modulus (cf. [34]) could not be seen from the present results (figure 10) with sufficient significance.

6. Summary

The absolute length of a silicon gauge block was investigated in a series of measurements at different temperatures and air pressures. From the collected dataset, the coefficient of thermal expansion α as well as the compressibility κ of silicon were derived. The evaluation is founded on a Bayesian model averaging approach to take different models and their possible errors additionally into account. While the uncertainties of the results reported previously [14] were estimated rather conservatively, the careful consideration of correlations lead to a reduction of the uncertainty presented in this work. For the CTE, standard uncertainties of less than 1×10^{-9} K^{-1} were achieved. These uncertainties are up to one order of magnitude smaller compared to the results reported previously [14]. In view of the data from [14] and this work, an update of the reference data recommended so far should be taken into consideration. The result of the compressibility is in agreement with data obtained by different measurement techniques described in the literature [17–19]. Moreover, it enables the resolution of the discrepancy in values reported in [16]. Ultimately, considering the achieved uncertainties, no significant dependence of the CTE on the actual pressure can be determined in the covered parameter space of temperature and pressure. As a consequence, it is permissible to apply the CTE value measured in vacuum for thermal expansion corrections of length measurements carried out in atmospheric pressure.

Acknowledgments

We thank our colleagues H H Ernst and F Lechelt for the careful preparation of the sample.

ORCID iDs

Guido Bartl https://orcid.org/0000-0002-0746-1200
Jörg Martin https://orcid.org/0000-0001-5066-7661
René Schödel https://orcid.org/0000-0002-7597-9036

References

[1] Enya K *et al* 2012 High-precision CTE measurement of hybrid C/SiC composite for cryogenic space telescopes *Cryogenics* **52** 86–9
[2] Hamann I, Sanjuan J, Spannagel R, Gohlke M, Wanner G, Schuster S, Guzman F and Braxmaier C 2019 Laser-dilatometer calibration using a single-crystal silicon sample *Int. Journal of Optomechatronics* **13** 18–29
[3] Mazur A V and Gasik M M 2009 Thermal expansion of silicon at temperatures up to 1100 °C *J. Mater. Process. Technol.* **209** 723–7
[4] Bureau Int. des Poids et Mesures 2019 *The Int. System of Units (SI) - Appendix 2: Practical realization of the definition of some important units* 9th edn (Sèvres: BIPM)
[5] White G K 1993 Reference materials for thermal expansion: certified or not? *Thermochimica Acta* **218** 83–99
[6] Swenson C A 1983 Recommended values for the thermal expansivity of silicon from 0 to 1000 K *J. Phys. Chem. Ref.* Data **12** 179–82
[7] Swenson C A, Roberts R B and White G K 1985 Thermal Expansion of Cu, Si, W, and Al_2O_3 *CODATA Bulletin* **59** 13–19
[8] Okada Y and Tokumaru Y 1984 Precise determination of lattice parameter and thermal expansion coefficient of silicon between 300 and 1500 K *J. Appl. Phys.* **56** 314–20
[9] Lyon K G, Salinger G L, Swenson C A and White G K 1977 Linear thermal expansion measurements on silicon from 6 to 340 K *J. Appl. Phys.* **48** 865–8
[10] Roberts R B 1981 Thermal expansion reference data: silicon 300-850 K *J. Phys.* D: *Appl. Phys.* **14** L163–L166
[11] Okaji M 1988 Absolute thermal expansion measurements of single-crystal silicon in the range 300–1300 K with an interferometric dilatometer *Int. J. Thermophys.* **9** 1101–9
[12] White G K and Minges M L 1997 Thermophysical properties of some key solids: An update *Int. J. Thermophys.* **18** 1269–327
[13] Watanabe H, Yamada N and Okaji M 2004 Linear thermal expansion coefficient of silicon from 293 to 1000 K *Int. J. Thermophys.* **25** 221–36
[14] Middelmann T, Walkov A, Bartl G and Schödel R 2015 Thermal expansion coefficient of single-crystal silicon from 7 K to 293 K *Phys. Rev.* B **92** 174113
[15] Karlmann P B, Klein K J, Halverson P G, Peters R D, Levine M B, Van Buren D and Dudik M J 2006 Linear thermal expansion measurements of single crystal silicon for validation of interferometer based cryogenic dilatometer *AIP Conf. Proc.* **824** 35–42
[16] Schödel R and Bönsch G 2001 Precise interferometric measurements at single crystal silicon yielding thermal expansion coefficients from 12 °C to 28 °C and compressibility. Jennifer E D and Nicholas B ed *Proc. SPIE: Recent Developments in Traceable Dimensional Measurements*, **4401** 54–62
[17] George A 1999 *Elastic Constants and Moduli of Diamond Cubic Si* (London: Inspec Publishing)
[18] McSkimin H J and Andreatch P 1964 Elastic moduli of silicon vs hydrostatic pressure at 25.0 °C and −195.8 °C *J. Appl. Phys.* **35** 2161–5
[19] Hall J J 1967 Electronic effects in the elastic constants of *n*-type silicon *Phys. Rev.* **161** 756–61

[20] Becker P, Bettin H, Danzebrink H-U, Gläser M, Kuetgens U, Nicolaus A, Schiel D, de Bièvre P, Valkiers S and Taylor P 2003 Determination of the Avogadro constant via the silicon route *Metrologia* **40** 271–87
[21] Martin J, Bartl G and Elster C 2019 Application of Bayesian model averaging to the determination of thermal expansion of single-crystal silicon *Meas. Sci. Technol.* **30** 045012
[22] Schödel R, Walkov A, Zenker M, Bartl G, Meeß R, Hagedorn D, Gaiser C, Thummes G and Heltzel S 2012 A new ultra precision interferometer for absolute length measurements down to cryogenic temperatures *Meas. Sci. Technol.* **23** 094004
[23] Schödel R 2015 Utilization of coincidence criteria in absolute length measurements by optical interferometry in vacuum and air *Meas. Sci. Technol.* **26** 084007
[24] Bartl G, Glaw S, Schmaljohann F and Schödel R 2019 Corrigendum: Correction for stress-induced optical path length changes in a refractometer cell at variable external pressure *Metrologia* **56** 049501
[25] Bartl G, Glaw S, Schmaljohann F and Schödel R 2019 Correction for stress-induced optical path length changes in a refractometer cell at variable external pressure *Metrologia* **56** 015001
[26] Tang S 1996 Self-calibrating five-frame algorithm for phase-shifting interferometry *Proc. SPIE* **2860** 91–8
[27] Schödel R 2007 Compensation of wavelength dependent image shifts in imaging optical interferometry *Appl. Opt.* **46** 7464–8
[28] Bönsch G, Schuster H-J and Schödel R 2001 Hochgenaue Temperaturmessung mit Thermoelementen (High-precision Temperature Measurements with Thermo Couples) *Technisches Messen* **68** 550–7
[29] Preston-Thomas H 1990 The temperature scale of 1990 *Metrologia* **27** 3–10
[30] Bönsch G and Potulski E 1998 Measurement of the refractive index of air and comparison with modified Edlén's formulae *Metrologia* **35** 133
[31] Schödel R, Walkov A, Voigt M and Bartl G 2018 Measurement of the refractive index of air in a low-pressure regime and the applicability of traditional empirical formulae *Meas. Sci. Technol.* **29** 064002
[32] Egan P F, Stone J A, Scherschligt J K and Harvey A H 2019 Measured relationship between thermodynamic pressure and refractivity for six candidate gases in laser barometry *J. Vacuum Science & Technology* A **37** 031603
[33] Murnaghan F D 1944 *The compressibility of media under extreme pressures: Proc. of the National Academy of Sciences*, **30** 244–7
[34] Garai J and Laugier A 2007 The temperature dependence of the isothermal bulk modulus at 1 bar pressure *J. Appl. Phys.* **101** 023514
[35] Robert R R and Wang K 1996 Thermal expansion and lattice parameters of group IV semiconductors *Mater. Chem. Phys.* **46** 259–64
[36] Ibach H 1969 Thermal expansion of silicon and zinc oxide (i) *Phys. Status Solidi* **31** 625–34
[37] Schödel R 2005 Accurate extraction of thermal expansion coefficients and their uncertainties from high precision interferometric length measurements *Recent Developments in Traceable Dimensional Measurements III* eds J E Decker and G-S Peng vol 5879 (Int. Society for Optics and Photonics, SPIE) 1–11
[38] Fischer J, de Podesta M, Hill K D, Moldover M, Pitre L, Rusby R, Steur P, Tamura O, White R and Wolber L 2011 Present Estimates of the Differences Between Thermodynamic Temperatures and the ITS-90 *Int. J. Thermophys.* **32** 12–25